



HAL
open science

Zwitterion functionalized gold nanoclusters for multimodal near infrared fluorescence and photoacoustic imaging

Danjin Shen, Maxime Henry, Vanessa Trouillet, Clothilde Comby-Zerbino, Franck Bertorelle, Lucie Sancey, Rodolphe Antoine, Jean-Luc Coll, Véronique Josserand, Xavier Le Guével

► **To cite this version:**

Danjin Shen, Maxime Henry, Vanessa Trouillet, Clothilde Comby-Zerbino, Franck Bertorelle, et al.. Zwitterion functionalized gold nanoclusters for multimodal near infrared fluorescence and photoacoustic imaging. *APL Materials*, 2017, 5 (5), pp.053404. 10.1063/1.4977203 . hal-02351327

HAL Id: hal-02351327

<https://hal.science/hal-02351327>

Submitted on 8 Nov 2019

HAL is a multi-disciplinary open access archive for the deposit and dissemination of scientific research documents, whether they are published or not. The documents may come from teaching and research institutions in France or abroad, or from public or private research centers.

L'archive ouverte pluridisciplinaire **HAL**, est destinée au dépôt et à la diffusion de documents scientifiques de niveau recherche, publiés ou non, émanant des établissements d'enseignement et de recherche français ou étrangers, des laboratoires publics ou privés.

Zwitterion functionalized gold nanoclusters for multimodal near infrared fluorescence and photoacoustic imaging

Danjin Shen¹, Maxime Henry¹, Vanessa Trouillet², Clothilde Comby-Zerbino³, Franck Bertorelle³, Lucie Sancey¹, Rodolphe Antoine³, Jean-Luc Coll¹, Véronique Josserand¹, Xavier Le Guével^{1*}

¹*Cancer Targets & Experimental Therapeutics, Institute for Advanced Biosciences (IAB), University of Grenoble Alpes (UGA)/ INSERM-U1209 / CNRS-UMR 5309- 38000 Grenoble, France*

²*Institute for Applied Materials (IAM) and Karlsruhe Nano Micro Facility (KNMF), Karlsruhe Institute of Technology (KIT), Eggenstein-Leopoldshafen, Germany*

³*Institut lumière matière, UMR5306, Université Claude Bernard Lyon1-CNRS, Université de Lyon 69622 Villeurbanne cedex, France*

Abstract

Gold nanoclusters (Au NCs) are an emerging type of theranostic agents combining therapeutic and imaging features with reduced toxicity. Au NCs stabilized by a zwitterion ligand with a fine control of the metal core size and the ligand coverage were synthesized by wet chemistry. Intense fluorescence signal is reported for the highest ligand coverage whereas photoacoustic signal is stronger for the largest metal core. The best Au NCs candidate with an average molecular weight of 17 kDa could be detected with high sensitivity on a 2D- NIR imaging instrument (LOD = 2.3 μ M) and by photoacoustic imaging. *In vitro* and *in vivo* experiments demonstrate an efficient cell uptake in U87 cell lines, a fast renal clearance ($t_{1/2\alpha} = 6.5 \pm 1.3$ min) and a good correlation between near

infrared fluorescence and photoacoustic measurements to follow the early uptake of Au NCs in liver.

Introduction

The sub-class of nanoclusters (NCs) in the wide library of metal nanoparticles have found a growing interest over the last few years for *in vivo* studies notably for cancer applications. Those metal NCs, mainly gold, are made of ten to hundred atoms and usually presented as species filling the gap between molecules and nanoparticles¹⁻⁴. Au NCs present several features making them appealing for cancer therapy thanks to i) their high renal clearance^{5,6} reducing toxicity risk, ii) the relatively high tumor retention by passive uptake^{7,8}, iii) the ability to trigger cell death under light illumination⁹ or radiosensitization¹⁰⁻¹², and iv) the detection by multimodal imaging techniques¹³⁻¹⁵.

In optical imaging, one of the great advantages of Au NCs compared to plasmonic Au NPs is related to the ability to visualize them by fluorescence in the red-NIR region (650-800 nm), a spectral window suitable for *in vivo* studies due to the reduced tissue scattering and low blood absorption^{16,17}. In addition, the high atomic number of gold ($Z=79$) allows a detection of gold particles by computed X-ray tomography (CT)⁵ and by photoacoustic imaging (PAI)^{18,19}. With the development of new contrast agents such as gold nanorods and nanocages, PAI combines the most compelling features of optical imaging and ultrasound imaging, providing both high optical contrast and high ultrasound resolution including *in vivo* in deep tissues²⁰⁻²².

Au NCs stabilized by glutathione (GSH) are probably one of the most described NCs in the literature with a precise control of their size and their structure²³⁻²⁶. The natural peptide GSH has a zwitterionic structure and, when coated on particle surface, could prevent the detection by macrophages²⁷. Recently, we investigated the optical properties and the behavior in cell environment of Au NCs stabilized by bidentate thiol zwitterionic ligand (Zw) which are highly stable Au NCs with intense fluorescence tunable in the near-infrared region²⁸⁻³⁰.

In this study, we aimed to determine the influence of the core size and the ligand coverage of gold particle to their fluorescence and their photoacoustic signals. For this purpose, gold particle of different size from the small plasmonic NPs (*i.e* size ~ 4 nm) to NCs (*i.e* size <2.5 nm) stabilized by a zwitterion ligand were prepared. Then, we investigated the behavior of the best candidate exhibiting both high fluorescence and photoacoustic signals in cells and in mice. Additional information are also reported on the NC size determined by mass spectrometry for Au NCs stabilized by zwitterionic ligand.

Materials and Methods

All products were purchased from Sigma Aldrich and MilliQ (Millipore, France) water was used for all experiments.

1- Particle synthesis.

Thioctic-zwitterion (Zw, C₁₅H₃₀N₂O₄S₃, M~399 g.mol⁻¹) was synthesized following the protocol described elsewhere²⁸. Au NCs with zwitterion (AuZw), were prepared by the addition of gold salt (HAuCl₄.3H₂O, 50 mM) to a basic solution (pH 10) containing the ligand in the presence of the strong reducing agent NaBH₄ (50mM) and stirred for 15 hours. Zwitterion stabilized Au NCs were synthesized with the molar ratio Au:Zw:NaBH₄ = 1:1:2, 1:2:2, and 1:5:2 molar ratio. Zwitterion stabilized Au NPs were synthesized with the molar ratio Au:Zw:NaBH₄ = 2:1:2, and 5:1:2. Afterwards, solutions were filtered twice with Amicon 3 kDa cut-off filters at 13,600 rpm for 20 min to remove excess free ligands, adjusted to pH 7, concentrated to 5 mg gold/mL in water and kept refrigerated until use.

Protected Au₂₅GSH₁₈ clusters were synthesized in two steps as described by T. Pradeep and co-workers³¹. Briefly in a first step, the complex formed between HAuCl₄ and glutathione GSH (Au:GSH= 1:4) was reduced in a methanolic solution (0°C) with NaBH₄. The resulting precipitate(Au@SG) was washed with methanol and dried. In a second step, Au@SG was dissolved

in water with 1mM of GSH and heated at 55°C for 12h. Solution was centrifuged and Au₂₅GSH₁₈ is precipitated from the supernatant by adding methanol. The precipitate was washed several time with methanol before drying in vacuum.

2- Instruments & techniques.

Transmission electron microscopy (TEM) images of the NCs and NPs were measured on a FEI Tecnai G2 Twin TEM. XPS investigation was performed in a K-Alpha+ spectrometer (ThermoFisher Scientific) using a microfocused, monochromated Al K α X-ray source (400 μ m spot size). The spectra were fitted with one or more Voigt profiles (BE uncertainty: ± 0.2 eV) and Scofield sensitivity factors were applied for quantification³². All spectra were referenced to the C1s peak at 285.0 eV binding energy (C–C, C–H) and controlled by means of the well-known photoelectron peaks of Cu, Ag, and Au, respectively. Measurements were performed on two different locations of dried samples. Evolution of the Au NC size as a function of the ratio metal–ligand was determined by electrospray ionization (ESI) on a commercial quadrupole time-of-flight (micro-qTOF, Bruker-Daltonics, Bremen, Germany, mass resolution $\sim 10,000$). The samples were prepared by diluting mother solution in water, to a final concentration of 0.25-0.5 mg.mL⁻¹ in 50/50% water/meOH v/v. The samples were analyzed in positive ion mode: each data point was the summation of spectra over 5 min. External calibration was carried out with a set of synthetic peptides.

Absorbance measurements on diluted samples were performed on a Evolution 201 (Thermoscientific) UV-vis spectrophotometer between 300 and 1000 nm. Fluorescence spectra were recorded on a Perkin Elmer LS45 Fluorescence Spectrometer. Fluorescence imaging was performed with a NIR 2D-Fluorescence Reflectance Imaging device (Fluobeam 800®, Fluoptics, France). The excitation is provided by a class 1 expanded laser source at 780 nm and the irradiance

on the imaging field is 100 mW/cm^2 . The fluorescence signal is collected by a CCD through a High pass filter with a high transmittance for wavelength $> 830 \text{ nm}$.

PAI was performed on The VevoLAZR system (Visualsonics, Fujifilm) using the LZ201 transducer (256 elements linear array; 9-18 MHz) allowing a $44 \mu\text{m}$ axial resolution. The laser is tunable between 680 and 970 nm and acquisitions can be made continuously with 1 nm steps providing a photoacoustic spectrum.

3- Cell experiments

U87MG cells were cultured in six-well plates one day before the experiment. The Au NCs were added to the cell medium at $50 \mu\text{g gold/mL}$ (eq. $35 \mu\text{M}$) for the indicated time (4 hours to 24 hours), and the cells were incubated at 37°C or 4°C . Then, the cells were resuspended with trypsin and carefully washed in PBS before analysis. Propidium Iodide was added to the cell suspension according to the manufacturer's instructions (BD Pharmingen, Belgium). The cells were analyzed using LSR II (Becton Dickinson, France). The 405 nm laser was used to excite the Au NCs, and the signal was collected after a long-pass 750 nm, at 780/60 nm. Propidium iodide was excited at 488 nm, filtered with the long-pass 655 nm, and its emission was collected at 660/20 nm. Specific compensations were applied to prevent the overlapping of the signals.

4- In vivo experiments

Six weeks old NMRI nude mice (Janvier, France) were anesthetized (air/isoflurane 4% for induction and 1.5% thereafter) and were injected intravenously via the tail vein with $200 \mu\text{L}$ of Au NCs at $600 \mu\text{M}$. *In vivo* fluorescence imaging was performed before and 1, 3, 5 and 24 hours after injection. Mice were euthanized at 1, 5 or 24 hours post injection ($n = 3$ mice per time point) and organs were harvested for *ex vivo* fluorescence imaging.

Three other mice were injected and blood samples were collected 10 sec and 5, 10, 15, 20, 30, 45

and 60 min after injection and were centrifuged (10 min at 2000 g) to separate plasma. Fluorescence imaging was then performed on plasma samples.

For PAI, an US gel (Parker Laboratories Inc., USA) was applied on the mouse body, the transducer was placed above the liver and a 30x30 mm² slice was imaged both in Bmode (ultrasound) and in PA mode at 710 nm before and 1, 5 and 24 hours after intravenous injection.

Results and Discussion

1- Characterization of Au NCs

We choose the ligand Zw (figure 1a) to produce gold particle of different size because this molecule was shown to strongly improve the colloidal stability of particle³³ and also to obtain Au NCs exhibiting one the highest fluorescence intensity reported so far^{28, 30, 34}. Molar ratio Au:Ligand has been modified during the synthesis in order to play both on the final metal core size and on the ligand coverage. Thus, a molar ratio Au > Ligand leads to NP for Au:Zw = 2:1 and 5:1 and a molar ratio Au ≤ Ligand leads to NCs for Au:Zw = 1:1, 1:2, and 1:5. TEM images (figure S1) show clearly a decrease of the metal core diameter when the amount of the ligand increases from 4.8±1.2 nm for Au:Zw 5:1 to less than 2.5 nm for Au:Zw 1:2 and Au:Zw 1:5. In the case of Au NCs (*i.e* for Au:Zw 1:1, Au:Zw 1:2 and Au:Zw 1:5), mass spectrometry is reckoned as suited technique to determine the full size and the structure of metal NCs³⁵⁻⁴⁰. We previously attempted to determine specific magic clusters using MALDI-Tof technique on those types of NCs without any success²⁸. Here, the high mass setting is optimized for the Au:Zw NCs. Au:Zw NCs contain multiple groups capable of being ionized and the ESI source can produce highly charged ions. For those molecules that can sustain multiple charges, a distribution of charge states is often observed in the mass-to-charge spectrum. This multiplicity of states gives rise to an “envelope” of peaks in the spectrum. The distribution of charges is observed in the m/z range 1000 - 8000 after electrospraying in positive mode water solution containing the nanoparticles (figure S2). Although the position of the peaks in the mass

spectra is stable, the relative abundance of the different peaks is found to be slightly dependent on the ESI-MS conditions. A multiplicative correlation algorithm (MCA) is used to estimate the mass of nanoparticles from the mass-to-charge spectra produced by electrospray ionization mass spectrometry⁴¹. The multiplicative correlation is designed to enhance the deconvoluted signal when the parent molecule is distributed into several charge states in the spectrum measured. This approach is summarized by the following formula⁴²:

$$f(m) = \prod_{z=z_0}^{z_1} g(m/z) / g_{rms}$$

where $f(m)$ is the intensity calculated in the spectrum for mass m , $g(m/z)$ is the intensity in the mass-to-charge spectrum, g_{rms} is the root-mean-square (rms) value of the signal measured.

As the Au NCs contain multiple ionized groups (Zw ligands), a distribution of charge states is observed in the mass-to-charge spectrum, and the MCA is used to estimate the mass of the Au NCs from the mass-to-charge spectra produced by the ESI-MS. As seen in figure 1b, for AuZw 1:1, the distribution is centered at 11000 Da with a second distribution (with a smaller intensity) at ~13500 Da. For AuZw 1:2, the mass increased to 17200 Da (with a second distribution with a smaller intensity at ~13600 Da). For AuZw 1:5, the mass reached to 32850 Da (with a second distribution at ~30660 Da and a third at ~28600 Da). Therefore, an obvious increase of the molecular weight of Au NCs occurs when the ligand content increases as previously reported²⁸. However in this study, we obtain a higher resolution in terms of size distribution thanks to the presence of an “envelope” of peaks in the spectrum and the multiplicative correlation algorithm designed to enhance the deconvoluted signal originated from the NCs. XPS experiments provide information about the atomic concentration of each element and the nature of interaction within the sample. Contribution of gold from the core bound directly to Zw *via* thiol groups and compared to the total amount of the ligand could be followed by looking at the energy binding of S 2p, in particular the component at 161,8 eV characteristic for S-Au (figure S3). In figure 1c, the ratio of gold concentration to the total

concentration of sulphur (Au/S_{total}) or to the concentration of sulphur bound to gold, hydrogen and to carbon ($Au/(S-Au+S-C+S-H)$) indicates a constant decrease when Zw increases. This behavior confirms that Zw continue to bind Au core even at the molar ratio $Au:Zw= 1:5$. Au_nZw_m stoichiometry is then evaluated based on the average mass estimated with deconvoluted ESI mass spectra and XPS results (giving access to Au/S ratio). Results show $m>n$ by a factor m/n higher than 2 for AuZw 1:1, AuZw 1:2, and AuZw 1:5, which is different for instance from the one reported for thiolated-protected clusters using glutathione⁴. Thus, the formation of AuZw could be seen rather like an organic charged layer coated onto ultra-small gold particles. Despite repetitive purification steps, the high reactivity of the bidentate thiotic group of Zw with gold and the strong electrostatic interaction inter-ligand due to the presence of the sulfonate and ammonium in Zw might prevent then the identification of magic size "superatom".

Absorbance measurements of AuZw sols show the standard plasmonic band at $\lambda= 520$ nm for AuZw 5:1 and AuZw 2:1 and usually observed for Au NPs with size above 3 nm¹. Increase of ligand content during the synthesis leads to the fall of the plasmonic band with a decrease of the UV band absorption (figure S4). We can see an isobectic point at $\lambda= 420$ nm between AuZw 1:2 and AuZw 1:5 that could be attributed to the absorption of the ligand Zw in the UV-visible region²⁸. Fluorescence (figure S5) is strongly enhanced when $Zw>Au$ with a rise at $\lambda= 820$ nm followed up by a blue-shift to $\lambda= 750$ nm like it was previously reported²⁸. Plasmonic NPs exhibit very weak or no fluorescence⁴³. However, AuZw 2:1 sample still presents some fluorescence signal despite the presence of a plasmon band. This effect could be related either to the presence of smaller NCs observed in HRTEM that cannot be separated to the NPs in the solution due to the low variation in weight or to the weak quenching effect of plasmonic NP due to the small particle size.

2- Phantom experiments

Fluorescence intensity of the aqueous AuZw sols (2 mg gold/mL) prepared at different molar ratio Au:Zw was measured on a NIR 2D-Fluorescence Reflectance Imaging device ($\lambda_{\text{exc.}}$ 780 nm; LP 830 nm). This medical device is dedicated to non-invasive or intraoperative *in vivo* imaging and has been used to guide surgical procedures^{44, 45}. Phantom imaging illustrated in figure 2a shows an exponential enhancement of the fluorescence intensity when increasing Zw content with the highest signal for AuZw 1:5, which is in agreement with the fluorescence measurements obtained on the spectrofluorimeter. The same trend is observed with a series of dilution up to 100 μg gold/mL from the concentrated AuZw sols to insure no self-absorption in this concentration window.

Photoacoustic signal of the different AuZw sols exhibit a similar profile (figure 2b) with a constant decrease of the intensity at longer wavelength from 680 nm to 910 nm followed by a slight augmentation until $\lambda=930$ nm and then decreases again. In figure 2c, photoacoustic signal of AuZw is plotted fixing the wavelength at $\lambda=710$ nm and drops drastically when Zw content increased especially between AuZw 2:1 and AuZw 1:1. Evolution of normalized fluorescence and photoacoustic signals is illustrated in figure 2d and shows an opposite trends with a stronger fluorescent signal for AuZw 1:5 whereas AuZw 5:1 exhibit the highest photoacoustic signal. This observation could be logically explained by the fact that high ligand coverage surrounding the metal core of the NCs improves the rigidity of the network leading to a strong fluorescence intensity⁴⁶. Inversely, particle with a bigger metal core like for AuZw 2:1 and AuZw 5:1 with size > 4 nm will produce heat under illumination leading to more intense vibration and then stronger photoacoustic signal.

We then decided to select the sample AuZw 1:2 as the optimal candidate for *in vitro* and *in vivo* experiments because it exhibits both quite intense fluorescence and enough signal to be detected by PAI. Knowing the molecular weight of AuZw 1:2 $\sim 17\text{kDa}$, and the weight concentration of gold per sample ($\sim 50\%$), AuZw concentration could be then expressed in M (mol/L) in this study. Fluorescence calibration of AuZw 1:2 between 4.5 μM to 600 μM suggests a limit of detection to

2.3 μM by fixing a signal/noise= 2 using PBS solution as control (figure 3a). This sensitivity can be considered as relatively high taking account of the low absorption of Au NCs at this excitation wavelength (see absorbance and fluorescence emission figures S4, S5). Photoacoustic calibration in figure 3b indicates a linear behaviour between 70 to 600 μM with signal >0.2 at 140 μM .

3- *In vitro* experiments

In vitro cell studies have been performed on glioblastoma cells in culture (U87MG) incubating those cells with AuZw 1:2 at 35 μM in complete medium during 4, 8, or 24 hours. Flow cytometry analysis illustrated in figure 4a indicates an enhancement of the fluorescent signal in cells originated from the Au NCs overtime (quantification reported in figure 4c) reaching more than 90% after 24 hours of incubation. Experiment performed at 4°C shows a very weak Au NC uptake in cells after 4 hours of incubation with less than 5% positive cells compared to the same experiment set at 37°C with 20.96% positive cells. This result confirms the low passive diffusion of those particles suggesting that AuZw 1:2 probably accumulates on the cell surface before an uptake by active process^{29, 30, 47}. Cytotoxicity assays have been performed using propidium iodide (figures 4b, 4c) and show no significant toxicity (<3%) until 24 hours incubation and even using Au NC concentration up to 100 μM (data no shown).

4- *In vivo* experiments

Blood pharmacokinetic of AuZw 1:2 (M~17 kDa; 600 μM in PBS) was measured by fluorescence imaging and shows a rapid clearance with an estimated half-life $t_{1/2\alpha} = 6.5 \pm 1.3$ min from a one compartment modelization. Wash out from blood is even faster using the well-characterized Au₂₅GSH₁₈ (M~11kDa)³¹ in the same condition with $t_{1/2\alpha} = 1.2 \pm 0.2$ min. Those estimated half-life values are in the same order than previous *in vivo* studies using Au NCs stabilized by the tripeptide

glutathione (GSH) reported by Zheng's team with $t_{1/2\alpha} = 5.4 \pm 1.2$ min with a NC size of 40 kDa⁸ and by Chen et al. with $t_{1/2\alpha} = 0.7 \pm 0.1$ min⁶. This indicates first that reducing particle's size drastically shortens the blood circulation and suggests also that the zwitterionic ligand Zw coated on Au NCs leads to a longer blood circulation than GSH looking at the entire particle size. Non-invasive *in vivo* fluorescence imaging confirms the high renal clearance with the strong accumulation of AuZw 1:2 in the bladder 1 hour after intravenous injection (figure 5b) in the same way that it was observed for others Au NCs^{6,7}.

We evaluated the biodistribution of AuZw 1:2 in liver by using fluorescence imaging (figures 6 a, c, e) and PAI (figures 6 b, d, e) 1, 3, 5, and 24 hours after intravenous injection. We found a good agreement between these two imaging techniques indicating an early accumulation of the Au NCs in the liver between 1 and 3 hours followed by a slow elimination until 24 hours. Mice were sacrificed at 1, 5, and 24 hours and biodistribution analysis from *ex vivo* fluorescence imaging illustrated in figure 6e shows the early elimination by kidney and bladder at 1 hour post injection which confirms the efficiency of kidney filtration for those Au NCs. The *ex vivo* data also indicate a weak fluorescence signal from all the other organs with the exception of the liver presenting an early uptake of Au NCs.

Conclusion

Herein, we demonstrate the ability to track gold nanoclusters (Au NCs) *in vivo* by two different imaging techniques based on 2D-NIR fluorescence and photoacoustic signal. Au NCs stabilized by a zwitterionic ligand could be synthesized by finely tuning metal core size/ligand coverage in order to provide the best compromise fluorescence/photoacoustic signals. Those Au NCs displayed high renal clearance and both imaging techniques indicate an early Au NC uptake in liver. Therefore, the

low toxicity and the detection of Au NCs by fluorescence imaging in the NIR region and by photoacoustic imaging make those contrast agents highly promising for future *in vivo* studies.

Supplementary materials: see the supporting information for the physico-chemical (TEM, XPS, ESI-MS) and optical (absorbance, fluorescence) properties of Au NCs.

Acknowledgements

Danjin Shen was financed by the Région Rhône Alpes (C³MIRA program). This work was realized at the small animal imaging technological platform OPTIMAL in the Institute of Advanced Biosciences (Grenoble, France). The Fluobeam800 fluorescence imaging device and the vevoLAZR photoacoustic imaging system were acquired thanks to France Life Imaging (FLI, French program “Investissement d'Avenir”; grant “Infrastructure d'avenir en Biologie Santé”, ANR-11-INBS-0006). The K-Alpha+ instrument was financially supported by the Federal Ministry of Economics and Technology on the basis of a decision by the German Bundestag.

References

1. Zhou, M.; Zeng, C.; Chen, Y.; Zhao, S.; Sfeir, M. Y.; Zhu, M.; Jin, R. Evolution from the plasmon to exciton state in ligand-protected atomically precise gold nanoparticles. *Nat. Commun.* 2016, 7.
2. Zheng, J.; Zhou, C.; Yu, M.; Liu, J. Different sized luminescent gold nanoparticles. *Nanoscale* 2012, 4, 4073-4083.
3. Jin, R. Quantum sized, thiolate-protected gold nanoclusters. *Nanoscale* 2010, 2, 343-362.
4. Jin, R.; Zeng, C.; Zhou, M.; Chen, Y. Atomically Precise Colloidal Metal Nanoclusters and Nanoparticles: Fundamentals and Opportunities. *Chem. Rev.* 2016, 116, 10346-10413.
5. Zhou, C.; Long, M.; Qin, Y.; Sun, X.; Zheng, J. Luminescent gold nanoparticles with efficient renal clearance. *Angew. Chem., Int. Ed. Eng.* 2011, 50, 3168-3172.
6. Chen, F.; Goel, S.; Hernandez, R.; Graves, S. A.; Shi, S.; Nickles, R. J.; Cai, W. Dynamic Positron Emission Tomography Imaging of Renal Clearable Gold Nanoparticles. *Small* 2016, 12, 2775-2782.
7. Liu, J.; Yu, M.; Zhou, C.; Yang, S.; Ning, X.; Zheng, J. Passive tumor targeting of renal-clearable luminescent gold nanoparticles: Long tumor retention and fast normal tissue clearance. *J. Am. Chem. Soc.* 2013, 135, 4978-4981.
8. Liu, J.; Yu, M.; Ning, X.; Zhou, C.; Yang, S.; Zheng, J. PEGylation and zwitterionization: Pros and cons in the renal clearance and tumor targeting of near-IR-emitting gold nanoparticles. *Angew. Chem., Int. Ed. Eng.* 2013, 52, 12572-12576.

9. Zhang, C.; Li, C.; Liu, Y.; Zhang, J.; Bao, C.; Liang, S.; Wang, Q.; Yang, Y.; Fu, H.; Wang, K.; Cui, D. Gold nanoclusters-based nanoprobe for simultaneous fluorescence imaging and targeted photodynamic therapy with superior penetration and retention behavior in tumors. *Adv. Funct. Mater.* 2015, 25, 1314-1325.
10. Zhang, X. D.; Luo, Z.; Chen, J.; Song, S.; Yuan, X.; Shen, X.; Wang, H.; Sun, Y.; Gao, K.; Zhang, L.; Fan, S.; Leong, D. T.; Guo, M.; Xie, J. Ultrasmall glutathione-protected gold nanoclusters as next generation radiotherapy sensitizers with high tumor uptake and high renal clearance. *Sci. Rep.* 2015, 5.
11. Zhang, X. D.; Luo, Z.; Chen, J.; Shen, X.; Song, S.; Sun, Y.; Fan, S.; Fan, F.; Leong, D. T.; Xie, J. Ultrasmall Au₁₀₋₁₂(SG)₁₀₋₁₂ nanomolecules for high tumor specificity and cancer radiotherapy. *Adv. Mat.* 2014, 26, 4565-4568.
12. Zhang, X. D.; Chen, J.; Luo, Z.; Wu, D.; Shen, X.; Song, S. S.; Sun, Y. M.; Liu, P. X.; Zhao, J.; Huo, S.; Fan, S.; Fan, F.; Liang, X. J.; Xie, J. Enhanced tumor accumulation of Sub-2 nm gold nanoclusters for cancer radiation therapy. *Adv. Healthcare Mater.* 2014, 3, 133-141.
13. Yahia-Ammar, A.; Sierra, D.; Mérola, F.; Hildebrandt, N.; Le Guével, X. Self-Assembled Gold Nanoclusters for Bright Fluorescence Imaging and Enhanced Drug Delivery. *ACS Nano* 2016, 10, 2591-2599.
14. Shang, L.; Stockmar, F.; Azadfar, N.; Nienhaus, G. U. Intracellular thermometry by using fluorescent gold nanoclusters. *Angew. Chem., Int. Ed. Engl.* 2013, 52, 11154-11157.
15. Le Guével, X. Recent advances on the synthesis of metal quantum nanoclusters and their application for bioimaging. *IEEE J. Sel. Top. Quantum Electron.* 2014, 20, 1-12.
16. Zhang, L.; Wang, E. Metal nanoclusters: New fluorescent probes for sensors and bioimaging. *Nano Today* 2014, 9, 132-157.
17. Shang, L.; Azadfar, N.; Stockmar, F.; Send, W.; Trouillet, V.; Bruns, M.; Gerthsen, D.; Nienhaus, G. U. One-pot synthesis of near-infrared fluorescent gold clusters for cellular fluorescence lifetime imaging. *Small* 2011, 7, 2614-2620.
18. Jokerst, J. V.; Thangaraj, M.; Kempen, P. J.; Sinclair, R.; Gambhir, S. S. Photoacoustic imaging of mesenchymal stem cells in living mice via silica-coated gold nanorods. *ACS Nano* 2012, 6, 5920-5930.
19. Zhang, Y. S.; Wang, Y.; Wang, L.; Wang, Y.; Cai, X.; Zhang, C.; Wang, L. V.; Xia, Y. Labeling human mesenchymal stem cells with gold nanocages for in vitro and in vivo tracking by two-photon microscopy and photoacoustic microscopy. *Theranostics* 2013, 3, 532-543.
20. Xia, J.; Yao, J.; Wang, L. V. Photoacoustic tomography: Principles and advances. *Prog. Electromagn. Res.* 2014, 147, 1-22.
21. Matthews, T. P.; Wang, K.; Wang, L. V.; Anastasio, M. A. In Synergistic image reconstruction for hybrid ultrasound and photoacoustic computed tomography, *Progress in Biomedical Optics and Imaging - Proceedings of SPIE*, 2015.
22. Wang, L. V.; Hu, S. Photoacoustic tomography: In vivo imaging from organelles to organs. *Science* 2012, 335, 1458-1462.
23. Yu, Y.; Luo, Z.; Chevrier, D. M.; Leong, D. T.; Zhang, P.; Jiang, D. E.; Xie, J. Identification of a highly luminescent Au₂₂(SG)₁₈ nanocluster. *J. Am. Chem. Soc.* 2014, 136, 1246-1249.
24. Wu, Z.; Chen, J.; Jin, R. One-pot synthesis of Au₂₅(SG)₁₈ 2- and 4-nm gold nanoparticles and comparison of their size-dependent properties. *Adv. Funct. Mat.* 2011, 21, 177-183.
25. Russier-Antoine, I.; Bertorelle, F.; Vojkovic, M.; Rayane, D.; Salmon, E.; Jonin, C.; Dugourd, P.; Antoine, R.; Brevet, P. F. Non-linear optical properties of gold quantum clusters. the smaller the better. *Nanoscale* 2014, 6, 13572-13578.
26. Negishi, Y.; Nobusada, K.; Tsukuda, T. Glutathione-protected gold clusters revisited: Bridging the gap between gold(I)-thiolate complexes and thiolate-protected gold nanocrystals. *J. Am. Chem. Soc.* 2005, 127, 5261-5270.

27. Larson, T. A.; Joshi, P. P.; Sokolov, K. Preventing protein adsorption and macrophage uptake of gold nanoparticles via a hydrophobic shield. *ACS Nano* 2012, 6, 9182-9190.
28. Le Guével, X.; Tagit, O.; Rodríguez, C. E.; Trouillet, V.; Pernia Leal, M.; Hildebrandt, N. Ligand effect on the size, valence state and red/near infrared photoluminescence of bidentate thiol gold nanoclusters. *Nanoscale* 2014, 6, 8091-8099.
29. Le Guével, X.; Perez Perrino, M.; Fernandez, T. D.; Palomares, F.; Torres, M. J.; Blanca, M.; Rojo, J.; Mayorga, C. Multivalent Glycosylation of Fluorescent Gold Nanoclusters Promotes Increased Human Dendritic Cell Targeting via Multiple Endocytic Pathways. *ACS Appl. Mater. Interfaces* 2015, 7, 20945-20956.
30. Fernandez, T. D.; Pearson, J. R.; Pernia Leal, M.; Torres, M. J.; Blanca, M.; Mayorga, C.; Le Guével, X. Intracellular accumulation and immunological properties of fluorescent gold nanoclusters in human dendritic cells. *Biomaterials* 2015, 43, 1-12.
31. Shibu, E. S.; Muhammed, M. A. H.; Tsukuda, T.; Pradeep, T. Ligand exchange of Au₂₅SG₁₈ leading to functionalized gold clusters: Spectroscopy, kinetics, and luminescence. *J. Phys. Chem. C* 2008, 112, 12168-12176.
32. Scofield, J. H. Hartree-Slater subshell photoionization cross-sections at 1254 and 1487 eV. *J. Electron Spectrosc. Relat. Phenom.* 1976, 8, 129-137.
33. Park, J.; Nam, J.; Won, N.; Jin, H.; Jung, S.; Jung, S.; Cho, S. H.; Kim, S. Compact and stable quantum dots with positive, negative, or zwitterionic surface: Specific cell interactions and non-specific adsorptions by the surface charges. *Adv. Func. Mat.* 2011, 21, 1558-1566.
34. Aldeek, F.; Muhammed, M. A. H.; Palui, G.; Zhan, N.; Mattoussi, H. Growth of highly fluorescent polyethylene glycol- and zwitterion- functionalized gold nanoclusters. *ACS Nano* 2013, 7, 2509-2521.
35. Hamouda, R.; Bellina, B.; Bertorelle, F.; Compagnon, I.; Antoine, R.; Broyer, M.; Rayane, D.; Dugourd, P. Electron emission of gas-phase [Au₂₅(SG)₁₈-6H]⁷⁻ gold cluster and its action spectroscopy. *J. Phys. Chem. Lett.* 2010, 1, 3189-3194.
36. Xu, Q.; Kumar, S.; Jin, S.; Qian, H.; Zhu, M.; Jin, R. Chiral 38-gold-atom nanoclusters: Synthesis and chiroptical properties. *Small* 2014, 10, 1008-1014.
37. Yu, Y.; Luo, Z.; Lee, J. Y.; Xie, J. Observation of cluster size growth in CO-directed synthesis of Au₂₅(SR)₁₈ nanoclusters. *ACS Nano* 2012, 6, 7920-7927.
38. Angel, L. A.; Majors, L. T.; Dharmaratne, A. C.; Dass, A. Ion mobility mass spectrometry of Au₂₅(SCH₂CH₂Ph)₁₈ nanoclusters. *ACS Nano* 2010, 4, 4691-4700.
39. Hamouda, R.; Bertorelle, F.; Rayane, D.; Antoine, R.; Broyer, M.; Dugourd, P. Glutathione capped gold Au_N(SG)_M clusters studied by isotope-resolved mass spectrometry. *Int. J. Mass Spectrom.* 2013, 335, 1-6.
40. Lu, Y.; Chen, W. Application of Mass Spectrometry in the Synthesis and Characterization of Metal Nanoclusters. *Anal. Chem.* 2015, 87, 10659-10667.
41. Truillet, C.; Lux, F.; Tillement, O.; Dugourd, P.; Antoine, R. Coupling of HPLC with electrospray ionization mass spectrometry for studying the aging of ultrasmall multifunctional gadolinium-based silica nanoparticles. *Anal. Chem.* 2013, 85, 10440-10447.
42. Hagen, J. J.; Monnig, C. A. Method for estimating molecular mass from electrospray spectra. *Anal. Chem.* 1994, 66, 1877-1883.
43. Link, S.; El-Sayed, M. A. Shape and size dependence of radiative, non-radiative and photothermal properties of gold nanocrystals. *Int. Rev. Phys. Chem.* 2000, 19, 409-453.
44. Atallah, I.; Milet, C.; Henry, M.; Jossierand, V.; Reyt, E.; Coll, J. L.; Hurbin, A.; Righini, C. A. Near-infrared fluorescence imaging-guided surgery improves recurrence-free survival rate in novel orthotopic animal model of head and neck squamous cell carcinoma. *Head & Neck* 2016, 38, E246-E255.
45. Jossierand, V.; Kéramidas, M.; Lavaud, J.; Righini, C.; Voltaire, J.; Bellard, E.; Rols, M. P.; Teissié, J.; Coll, J. L.; Golzio, M. Electrochemotherapy guided by intraoperative fluorescence

imaging for the treatment of inoperable peritoneal micro-metastases. *J. Controlled Release* 2016, 233, 81-87.

46. Pyo, K.; Thanthirige, V. D.; Kwak, K.; Pandurangan, P.; Ramakrishna, G.; Lee, D. Ultrabright Luminescence from Gold Nanoclusters: Rigidifying the Au(I)-Thiolate Shell. *J. Am. Chem. Soc.* 2015, 137, 8244-8250.

47. Yang, L.; Shang, L.; Nienhaus, G. U. Mechanistic aspects of fluorescent gold nanocluster internalization by live HeLa cells. *Nanoscale* 2013, 5, 1537-1543.

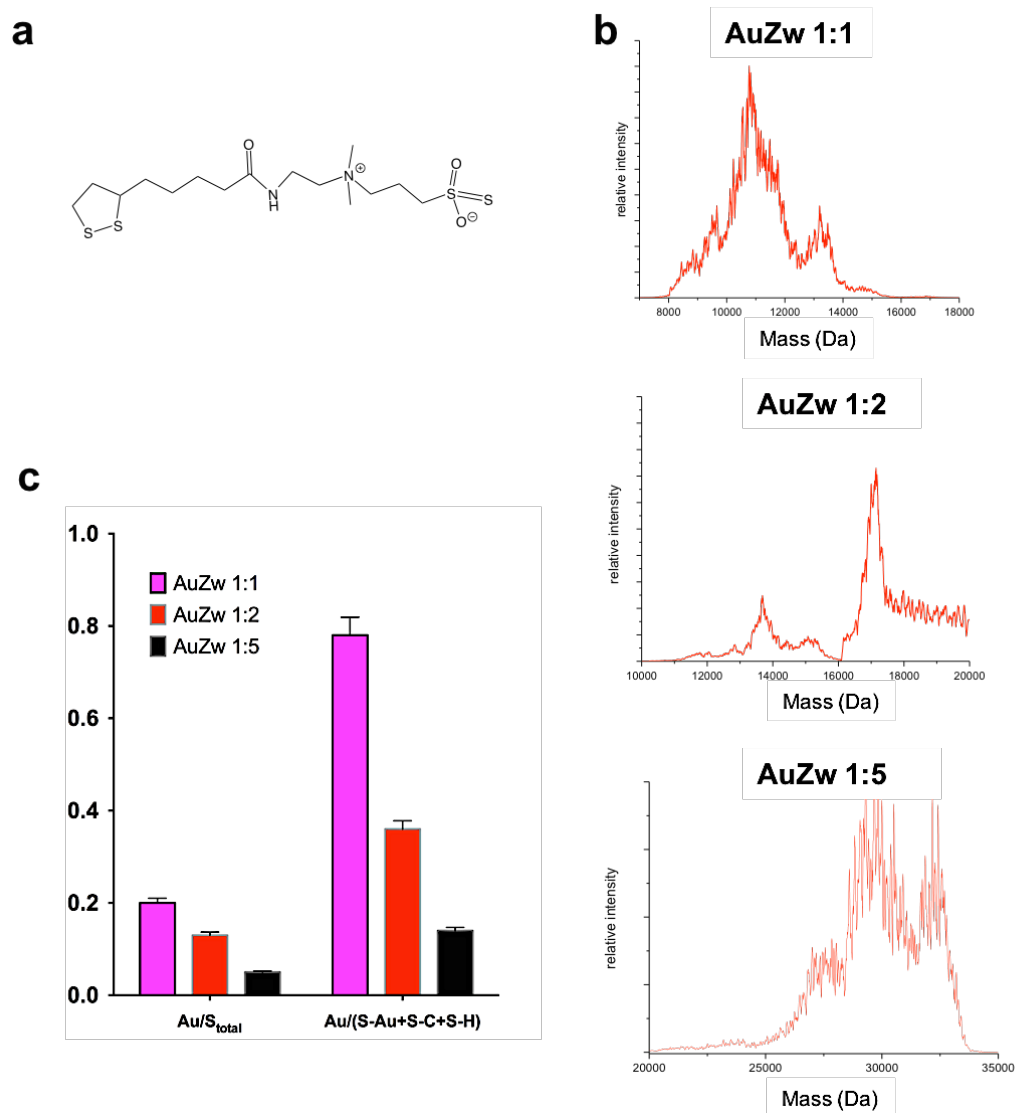


Figure 1. (a) Chemical formula of the thioctic bidentate zwitterionic ligand Zw. (b) Deconvoluted ESI MS spectra of AuZw 1:1, AuZw 1:2, and AuZw 1:5. (c) Concentration of gold (atomic%) with respect to total concentration sulphur (S_{total}) or to sulphur bind to gold, carbon and thiol (S-Au+S-C+S-H) from Zw extracted from XPS measurements.

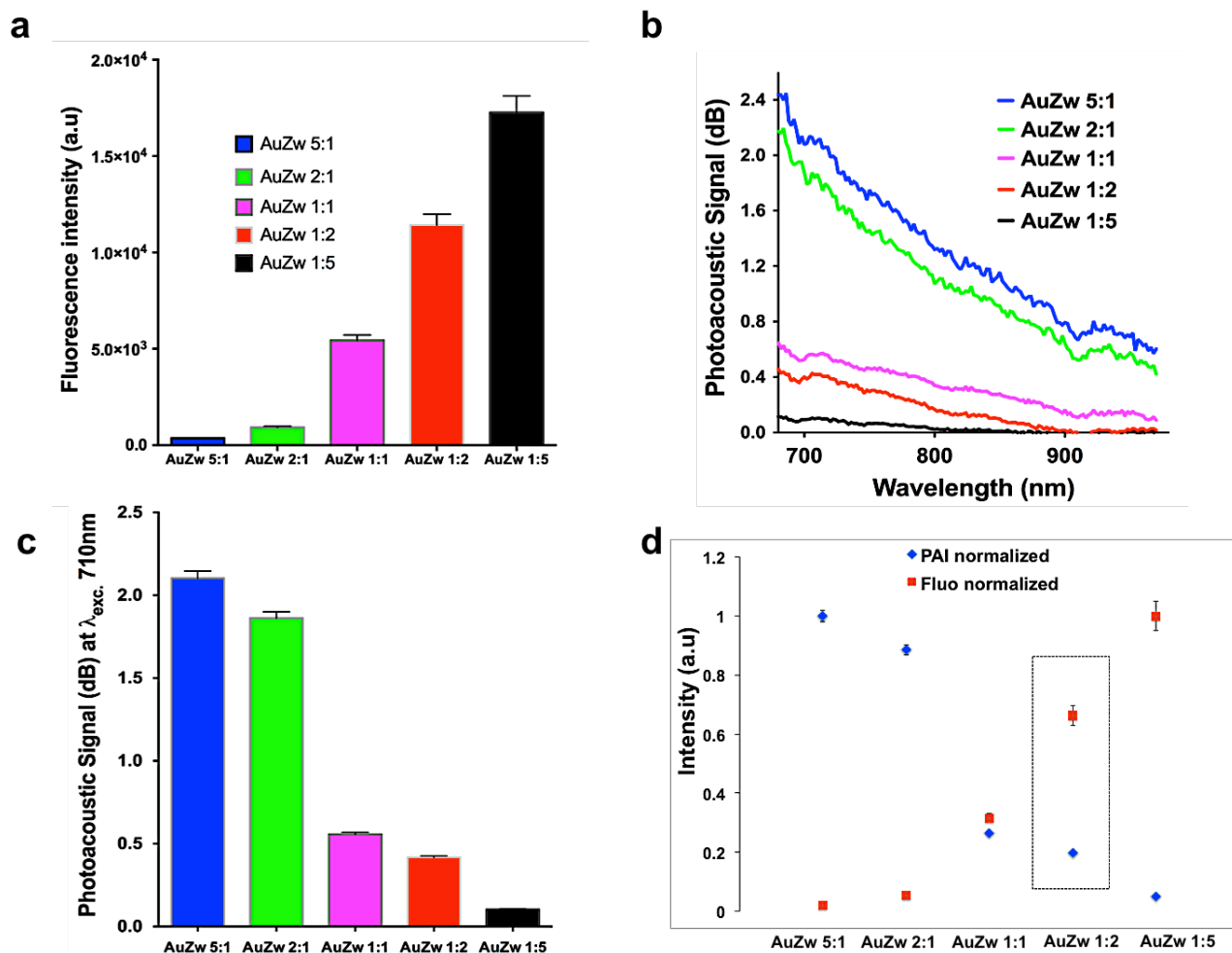


Figure 2. (a) Fluorescence intensity of AuZw sols (2 mg gold/mL) measured with a NIR 2D-Fluorescence Reflectance Imaging device ($\lambda_{exc.}$ 780 nm; LP 830 nm). Photoacoustic signal of AuZw sols (2 mg gold/mL) (b) between 690 and 970 nm and (c) at $\lambda_{exc.}$ 710 nm. (d) Normalized fluorescence and photoacoustic signals for AuZw (2 mg gold/mL).

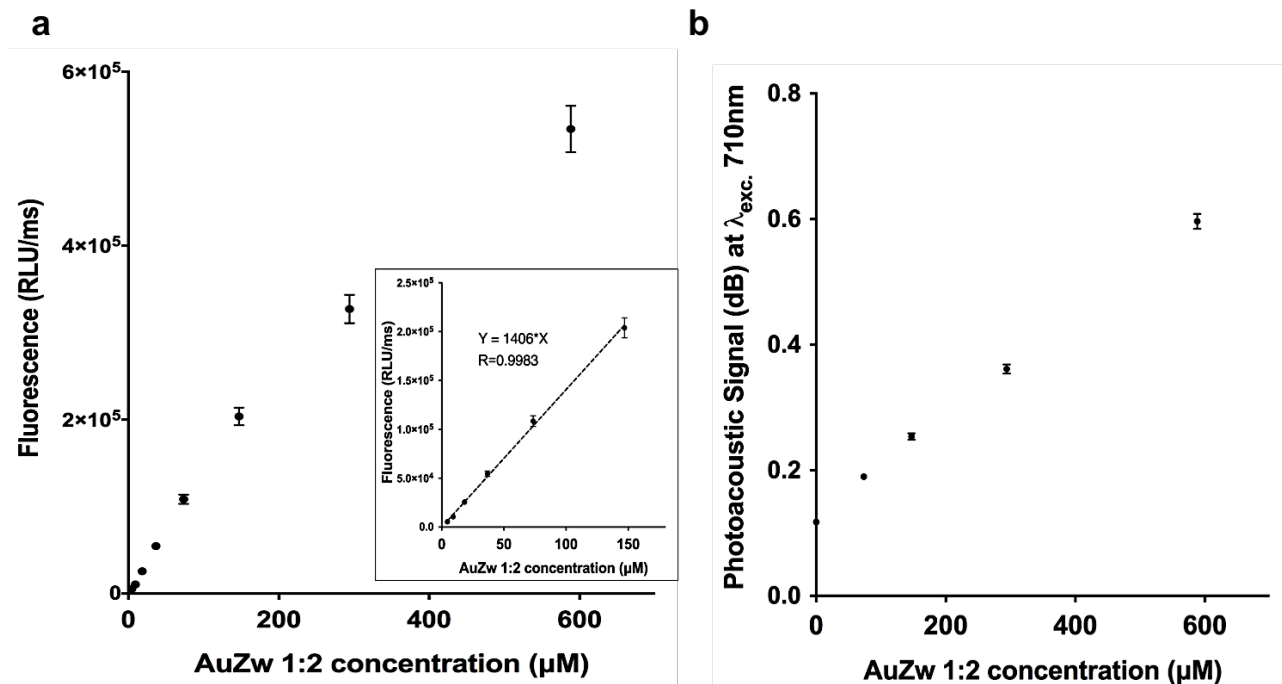


Figure 3. (a) Calibration of AuZw 1:2 fluorescence intensity between 4.5 to 600 μM in water measured with a NIR 2D-Fluorescence Reflectance Imaging device ($\lambda_{\text{exc.}}$ 780 nm; LP 830 nm). (b) Calibration of AuZw 1:2 photoacoustic signal between 70 and 600 μM in water.

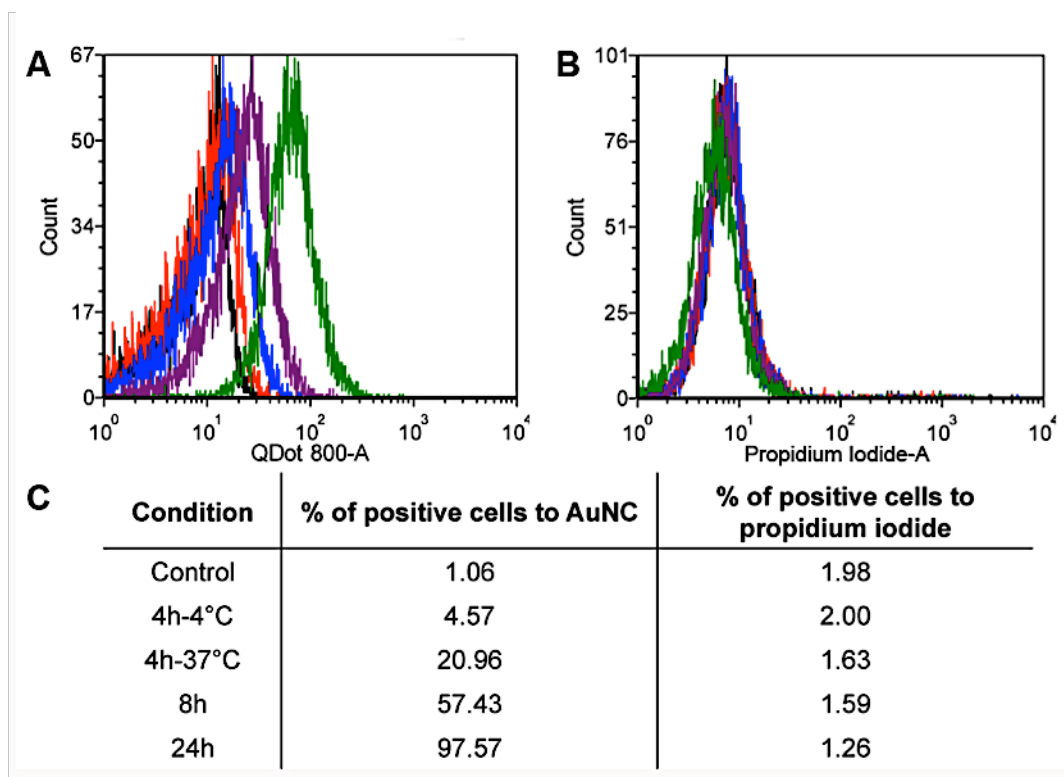


Figure 4. (a, c) Flow cytometry results and (b, c) toxicity tests by propidium iodide on U87MG cells incubated with AuZw 1:2 (35 μ M in complete medium) at different time points and at 37°C and at 4°C for 4 hours.

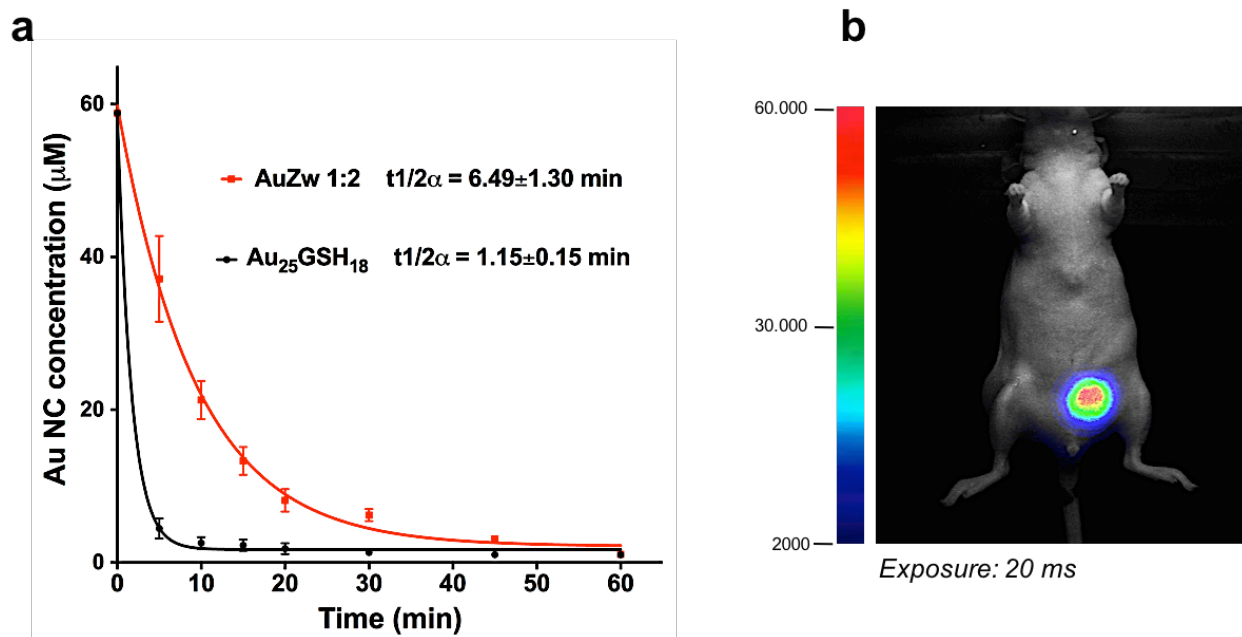


Figure 5. (a) Blood pharmacokinetic of AuZw 1:2 and Au₂₅GSH₁₈ after intravenous injection (200 μL ; 600 μM). Au NC concentration is determined from the fluorescence intensity values. (b) Non-invasive *in vivo* 2D fluorescence imaging 1 hour after intravenous injection of AuZw 1:2 (600 μM , $V = 200$ μL) illustrating the strong elimination of Au NC by the bladder.

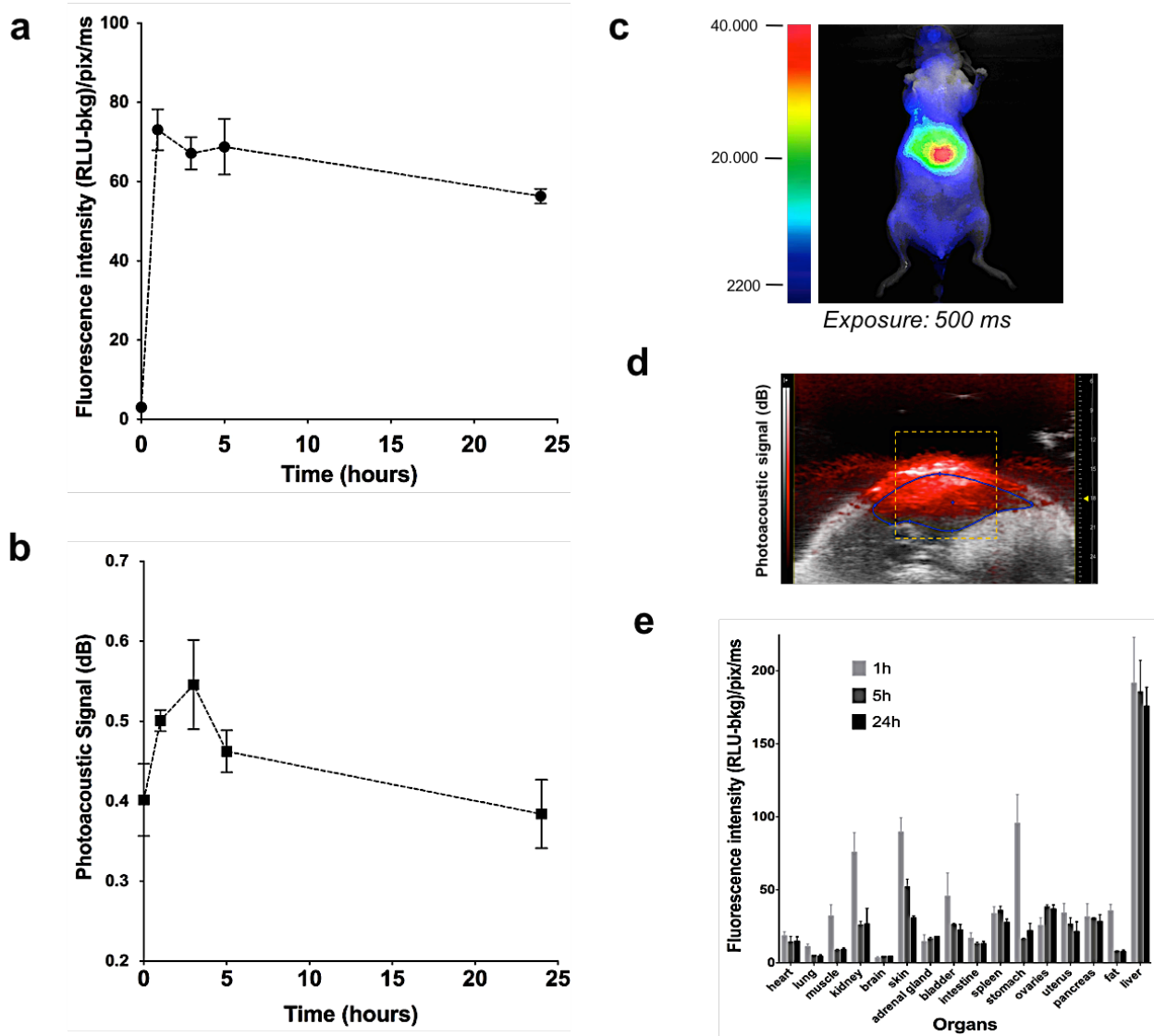


Figure 6. Kinetic of AuZw 1:2 uptake in liver by (a) fluorescence and (b) photoacoustic imaging. (c) Non-invasive *in vivo* fluorescence (left) and (d) photoacoustic (right) imaging 3 hours after AuZw 1:2 intravenous injection (200 μ L; 600 μ M). (e) Biodistribution analysis from *ex vivo* fluorescence imaging in different organs 1 hour, 5 hours, and 24 hours after Au NC intravenous injection (200 μ L; 600 μ M).